Research Article

Ashour M. Ahmed, Doaa Essam, Mohamed A. Basyooni-M. Kabatas*, Ahmed A. Abdel-Khaliek, Mohamed Shaban, Mamduh J. Aljaafreh, and Mohamed Rabia

Synthesis and electrochemical characterization of iron oxide/poly(2-methylaniline) nanohybrids for supercapacitor application

https://doi.org/10.1515/ntrev-2025-0189
received February 10, 2025; accepted June 10, 2025

Abstract: This study reports the synthesis of a nanohybrid material composed of poly(2-methylaniline) (P(2MA)) and iron oxide (Fe_2O_3) as electrodes for supercapacitors using a simple and cost-effective method. Various characterization techniques were employed to analyze the samples. The results revealed that the Fe_2O_3/P(2MA) nanohybrid exhibits nanofiber structures, while pure P(2MA) displays a porous hollow sphere morphology. Furthermore, the analysis confirmed the effective dispersion of Fe_2O_3 nanoparticles within the polymer matrix. The electrochemical properties of the Fe_2O_3/P(2MA) nanohybrid were found to surpass those of pure P(2MA) in both NaCl and HCl electrolytes. Notably, the nanohybrid demonstrated longer discharge times and higher oxidation/reduction currents in HCl than NaCl. The gravimetric and areal capacitances were measured at 998.4 F g^{-1} and 1497.6 mF cm^{-2} in 0.5 M HCl at a current density of 0.6 A g^{-1}. Furthermore, the nanohybrid retained 99.9% of its initial specific capacitance after 2,000 cycles. These findings underscore the significant potential of the Fe_2O_3/P(2MA) nanohybrid as a high-performance supercapacitor electrode for energy storage applications.

Keywords: poly(2-methylaniline), Fe_2O_3, Fe_2O_3/P(2MA) nanohybrid, supercapacitor, electrolyte, specific capacitance

1 Introduction

Currently, electrochemical supercapacitors (ECs) have a wide range of modern applications [1–3]. Supercapacitors can be categorized into electric double-layer capacitors (EDLCs) and pseudocapacitors (PCs) based on the different electrochemical energy storage mechanisms they employ [4,5]. EDLCs utilize carbon-based materials such as graphene and activated carbon as electrodes, enabling reversible adsorption and desorption of ions at the electrode–electrolyte interface [6,7]. The charge storage primarily occurs within the electric double layer formed at this interface. The high specific surface area, good electrical conductivity, and mechanical stability of carbon-based EDLC materials have attracted significant research interest [8,9]. However, these materials often suffer from high internal resistance and relatively low capacitance, which restricts their broader application [10]. PCs store energy through quick and reversible Faradaic interactions at the surface of active electrodes. Conducting polymers (CPs) have been extensively studied as potential materials for PCs, including polypyrrole (PPy), polyindole, poly(3,4-ethylenedioxythiophene), polyaniline (PANI), and poly(2-methyl aniline) (P(2MA)) [11,12–18]. However, CPs often suffer from cycling instability due to the swelling and shrinking of the polymeric chains during the charging–discharging process [19]. Metal oxides (MOs) and metal sulfides investigated as supercapacitor electrodes include CoS, PbS, RuO_2, NiO, Al_2O_3, TiO_2, MnO_2, Mn_3O_4, and V_2O_5 [19–23]. Although MOs offer specific energy and capacitance advantages, they suffer from low conductivity and are prone to easy agglomeration during interactions [24]. Many researchers have investigated blending conductive polymers

* **Corresponding author: Mohamed A. Basyooni-M. Kabatas,** Department of Precision and Microsystems Engineering, Delft University of Technology, Mekelweg 2, 2628 CD, Delft, Netherlands; Department of Nanotechnology and Advanced Materials, Graduate School of Applied and Natural Science, Selçuk University, Konya 42030, Turkey, e-mail: m.kabatas@tudelft.nl, m.a.basyooni@gmail.com
Ashour M. Ahmed, Mamduh J. Aljaafreh: Physics Department, College of Science, Imam Mohammad Ibn Saud Islamic University (IMSIU), Riyadh, 11623, Saudi Arabia
Doaa Essam, Ahmed A. Abdel-Khaliek: Physical Chemistry Laboratory, Chemistry Department, Faculty of Science, Beni-Suef University, Beni-Suef, 62514, Egypt
Mohamed Shaban: Physics Department, Faculty of Science, Islamic University of Madinah, Madinah, Saudi Arabia
Mohamed Rabia: Nanomaterials Science Research Laboratory, Chemistry Department, Faculty of Science, Beni-Suef University, Beni-Suef, 62521, Egypt

with MOs to address these limitations. The combination of CPs/MOs is promising for improving electrical conductivity and enabling fast, reversible redox reactions with enhanced specific capacitance [25,26]. In this context, Fathy *et al.* used cobalt nickel oxide combined with poly(*m*-toluidine) as an electrode material to enhance supercapacitor performance [27]. Bathula *et al.* reported that poly(3-dodecylthiophene)-wrapped cobalt oxide (P3DDT-Co_3O_4) exhibited a specific capacitance of 294 F g^{-1}, substantially higher than that of pristine Co_3O_4 (174 F g^{-1}) at a current density of 1 A g^{-1} [28]. Chenyang *et al.* described 3D-structured $NiCo_2O_4$-PANI nanosheets as a standing electrode for supercapacitors, delivering a higher specific capacitance than $NiCo_2O_4$ alone [29]. Additionally, Merlin *et al.* presented Ag_2WO_4 and an Ag_2WO_4/PANI nanocomposite as supercapacitor electrodes, with the Ag_2WO_4/PANI nanocomposite showing about five times the capacitance of Ag_2WO_4 alone [30]. In these works, the capacitance remains relatively low and requires further improvements for better supercapacitor performance.

On the other hand, P(2MA) is a promising CP derived from the monomer *m*-toluidine through oxidative polymerization. It belongs to the polyaniline family and shares many similar properties. Notably, P(2MA) exhibits electrical conductivity due to the delocalization of electrons along its polymer chain, facilitating the flow of electric charge. The electron-donating methyl group on its phenyl ring lowers resistance and enhances capacitance [31]. Moreover, these methyl groups contribute additional electrons, increasing the surface area of the electroactive sites, enhancing polymer stability, and accelerating the charging and discharging processes [32,33]. P(2MA) also demonstrates advantageous characteristics such as high stability, resistance to oxidation, reversible redox reactions, intense absorption in the visible region, and mechanical flexibility. These attributes make P(2MA) suitable for diverse applications, including optoelectronic systems, electrochemical devices, hydrogen generation, sensors, and conductive coatings [27,31,32,34,35]. However, despite its promising qualities, its potential as an energy storage electrode for supercapacitors remains underexplored.

Iron oxide (Fe_2O_3) nanoparticles have gained considerable attention for their potential in supercapacitors, fuel cells, electronic devices, and photocatalysis [36]. Iron oxide offers notable advantages such as cost-effectiveness, abundant availability, and environmental friendliness [37,38]. Its suitability for supercapacitor electrodes is attributed to its high theoretical capacity and the ability to exist in multiple oxidation states. Vittaya *et al.* developed flower-shaped Fe_2O_3 nanomaterials as supercapacitor electrodes, achieving a capacitance of 218.49 F g^{-1} at 1 A g^{-1} [39]. Wang *et al.* fabricated trigonal α-Fe_2O_3 structures *via* high-temperature thermal decomposition, resulting in a specific capacitance of 149.3 F g^{-1} at 1 A g^{-1} [40]. Saxena *et al.* synthesized Fe_2O_3 nanocubes with a specific capacitance of 288 F g^{-1} at 1 A g^{-1} [41]. Similarly, Surender *et al.* examined Fe_2O_3 nanomaterials as supercapacitor electrodes, achieving a capacitance of approximately 123 F g^{-1} at 1 A g^{-1} [42]. Nevertheless, Fe_2O_3 exhibits drawbacks, including poor Coulombic efficiency and rapid capacity decay during charge–discharge cycles [43,44]. Its limited electrical conductivity and moderate specific capacitance have also restricted its broader adoption in supercapacitor technologies.

It is expected that incorporating Fe_2O_3 into the P(2MA) matrix to form a Fe_2O_3/P(2MA) nanohybrid will effectively address the limitations of both materials for supercapacitor applications. This integration enhances the contact between the nanohybrid and the current collector, improving overall electrical conductivity [45,46]. Additionally, it expands the surface area available for the reversible redox faradaic reactions. The synergistic effects of the Fe_2O_3/P(2MA) nanohybrid result in several benefits, such as facilitating more effective charge transfer and increased stability over longer-term operations.

Most researchers initially synthesized MO nanoparticles and then incorporated them into polymer chains during polymerization to fabricate nanocomposites [27,47,48]. This study uses a one-pot photopolymerization approach to develop Fe_2O_3/P(2MA) nanohybrids for supercapacitor applications. A key innovation lies in combining photopolymerization with chemical oxidative polymerization, enabling efficient, controllable synthesis. In this method, $FeCl_3$ serves a dual role as the oxidizing agent and the precursor for *in situ* Fe_2O_3 nanoparticle formation, facilitating the direct construction of a nanofibrous Fe_2O_3/P(2MA) nanohybrid. P(2MA), as an alternative to the widely studied polyaniline, takes advantage of its high electrical conductivity, thermal stability, and ease of processing. The resulting nanohybrid features uniform Fe_2O_3 dispersion and strong polymer–oxide interfacial bonding, forming a porous, high-surface-area architecture that improves ion diffusion and charge transport. This synergistic structure significantly boosts specific capacitance and cycling stability. Additionally, the single-step, cost-effective, and environmentally friendly method eliminates the need for separate oxidants and reduces fabrication complexity compared to traditional multi-step procedures.

The characteristics of both pure P(2MA) and Fe_2O_3/P(2MA) nanohybrids were analyzed using several characterization techniques, including X-ray diffraction (XRD), Fourier transform infrared spectroscopy (FTIR), X-ray photoelectron spectroscopy (XPS), scanning electron microscopy (SEM), and UV spectroscopy. The electrochemical performance of the nanohybrid electrode was evaluated using different aqueous electrolytes, specifically NaCl and HCl. After 2,000 charge/discharge cycles, the Fe_2O_3/P(2MA) nanohybrid exhibited high stability in HCl electrolytes.

2 Experimental section

2.1 Synthesis of the P(2MA) nanopowder

The pure P(2MA) nanopowder was synthesized using the photopolymerization method. Initially, a solution of 0.12 M *m*-toluidine ($C_6H_4CH_3NH_2$) and 0.5 M acetic acid (CH_3COOH) was stirred, while a separate solution of 0.12 M potassium persulfate (KPS) dissolved in 0.5 M CH_3COOH acted as the oxidizing agent. The two solutions were then combined and stirred for 2 h. Next, the resulting mixture was exposed to UV light for 15 h to ensure complete polymerization. The mixture was filtered to obtain the pure P(2MA) nanopowder and was finally dried at 70°C.

2.2 Synthesis of the Fe_2O_3/P(2MA) nanohybrid

The synthesis of the Fe_2O_3/P(2MA) nanohybrid followed a slightly different procedure. Initially, 0.12 M *m*-toluidine was dissolved in 0.5 M acetic acid to create a solution. Simultaneously, another solution was prepared, containing 0.12 M iron chloride hexahydrate ($FeCl_3.6H_2O$) and 0.5 M acetic acid. Equimolar concentrations of 0.12 M $FeCl_3{\cdot}6\ H_2O$ and 0.12 M *m*-toluidine were intentionally selected to balance the redox capacity of Fe_2O_3 with the electrical conductivity of P(2MA). An excessive amount of Fe_2O_3 can hinder electron transport and promote nanoparticle aggregation, while an overabundance of the polymer may dilute redox-active sites and reduce overall capacitance [11,22]. This equimolar ratio thus represents a near-optimal compromise, resulting in high specific capacitance and excellent cycling stability. These two solutions were then mixed for 2 h. Subsequently, the combined solutions were exposed to UV light for 15 h. Finally, the mixture was filtered, purified, and dried overnight at 70°C to obtain the Fe_2O_3/P(2MA) nanohybrid. Based on the initial molar concentrations and accounting for Fe_2O_3 formation (0.06 mol × 159.69 g/mol ≈ 9.58 g) and polymer yield (≈12.86 g), the final mass ratio of Fe_2O_3 was approximately 43 wt% of the nanohybrid.

2.3 Characterization of the synthesized nanostructures

Characterization of the synthesized nanostructures involved several techniques to assess their properties. The morphological features were observed using an SEM (Axioskop 40 POL, Zeiss) and a transmission electron microscope (TEM, JOEL JEM-2010). The compositional structure properties of both the pure P(2MA) nanopowder and the Fe_2O_3/P(2MA) nanohybrid were analyzed using X-ray diffraction (XRD, Philips X'Pert Pro MRD) and Fourier-transform infrared spectroscopy (FTIR, Bruker Vertex 70). A UV-Vis spectrophotometer (Lambda 950, Perkin Elmer) was employed to investigate the optical characteristics. Furthermore, XPS (Axis Ultra DLD) was performed to evaluate the elemental state of the nanostructures.

2.4 Supercapacitor design

To create a well-mixed catalyst ink, 250 µg of active nanopowder material (P(2MA) or Fe_2O_3/P(2MA)) and 25 µg of graphite nanopowder were combined with 0.350 mL of ethanol and 0.050 mL of Nafion. The resulting mixture was then vigorously shaken in a sealed bottle for 1 day to ensure thorough homogenization. Collectors currently employ two gold (Au) sheets. Au was selected for its high electrical conductivity and chemical stability, ensuring no reaction with the electrolytes. The current collector played a vital role in a supercapacitor by facilitating efficient electron transfer between the external circuit and electrode materials during the charge and discharge processes [49]. It ensures uniform current distribution across the electrode surface.

Additionally, it provides mechanical support to the electrode materials and aids in dissipating heat generated during operation. Approximately 56.0 µL of the homogeneous slurry was carefully applied to etch the Au sheets (1 cm^2). Two pieces of filter paper were immersed in separate solutions overnight. One piece was soaked in a 0.5 M sodium chloride (NaCl) electrolyte, while the other was submerged in a 0.5 M hydrochloric acid (HCl) electrolyte. A strip of electrolyte-soaked filter paper was inserted between the two newly constructed electrodes to design the supercapacitor device.

2.5 Electrochemical description

Various electrochemical tests were conducted using an electrochemical workstation (CHI 660E; CH Instruments, China) to evaluate the performance of the pure P(2MA) and Fe_2O_3/P(2MA) nanohybrid. Galvanostatic charge/discharge (GCD) measurements were performed at different current densities in different aqueous electrolyte solutions.

Cyclic voltammetry (CV) experiments were conducted at various scan rates within a voltage window ranging from 0 to 1 V.

3 Results and discussion

3.1 Morphological and structural section

SEM was employed to analyze the morphological features of both pure P(2MA) and the Fe_2O_3/P(2MA) nanohybrid, as shown in Figure 1. The SEM image (Figure 1a) revealed that pure P(2MA) exhibited spherical shapes with hollow interior structures. The surfaces of these hollow spheres were open and featured small holes. Similar structures have been observed in previous studies for polymers such as poly(*o*-toluidine) and polyaniline when KPS or ammonium persulfate were used as oxidants [50,51]. Figure S1 clearly illustrates these hollow spheres with surface holes. The hole sizes ranged from 0.2 to 0.35 µm, while the hollow sphere diameters ranged from 0.5 to 0.9 µm. The hollow interior in these spheres allows solutions to penetrate inside. The morphology of porous hollow sphere nanoparticles is helpful for various applications where solution infiltration or encapsulation is desired.

SEM micrographs of the Fe_2O_3/P(2MA) nanohybrid (Figure 1b) illustrate the formation of a spongy and irregularly accumulated structure of nanofibers. This structure indicates an improved attachment of Fe_2O_3 to the P(2MA) chain. The corresponding microstructure exhibits highly desirable characteristics for energy storage systems [52]. The presence of aggregated porosity areas enhances electrical conductivity because when a material has aggregated porosity, a network of interconnected pores is formed. This arrangement can significantly improve electrical conductivity by providing several channels for electron transport [53–57]. Nanofiber-based materials reduce the ion diffusion pathway, enabling faster ion intercalation kinetics [58]. The high surface area of the spongy structure helps decrease charge-transfer resistance at the electrode/electrolyte interface [59,60].

The transition from KPS to $FeCl_3$ plays a critical role in driving the morphological shift from hollow spheres in pure P(2MA) to spongy nanofibers in Fe_2O_3/P(2MA) during photopolymerization [61]. This transformation is multifactorial and complex. In pure P(2MA) synthesis, KPS functions solely as a source of sulfate radicals that initiate the polymerization process, without exerting significant templating or structural influence. However, since 2MA dissolves in acid, some monomer droplets are dispersed across the surface, and their oxidation in the presence of KPS leads to the formation of hollow spheres *via* the water-in-oil method [50,51,62]. In contrast, $FeCl_3$ in the Fe_2O_3/P(2MA) nanohybrid serves a dual function: it acts as an oxidizing agent and a precursor for the *in situ* generation

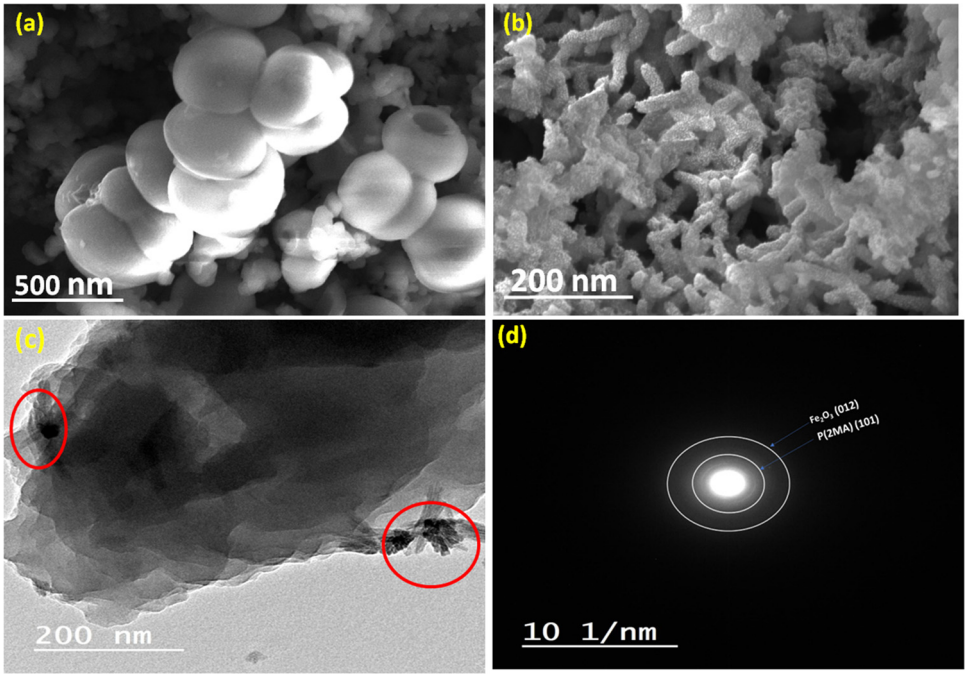

Figure 1: SEM images of (a) pure P(2MA), (b) Fe_2O_3/P(2MA) nanohybrid, (c) TEM micrograph, and (d) SAED of Fe_2O_3/P(2MA).

of Fe_2O_3 nanoparticles [63]. These photochemically generated nanoparticles serve as coordination-templating sites that guide polymer growth into one-dimensional fibers through strong polymer–nanoparticle interactions [64]. The simultaneous formation of the polymer and MO phases creates a dynamic reaction environment fundamentally distinct from the pure polymer system. Changes in solvent polarity, viscosity, ionic strength, and pH induced by $FeCl_3$ influence polymer chain behavior, modifying the propagation mechanism during growth and altering the polymerization kinetics. This favors linear propagation and suppresses the cross-linking processes that typically lead to the formation of closed hollow spheres. Additionally, introducing Fe^{3+} ions facilitates the formation of coordination complexes with the amine groups in the monomer [65]. Therefore, the observed morphological transition is likely the result of a synergistic interplay among the oxidizing agent, nanoparticle formation, and polymer–MO interactions, rather than the effect of the oxidizing agent alone [66].

The TEM morphology of the nanohybrid is presented in Figure 1c. The TEM image reveals nanofibers of the nanohybrid at the edges, as indicated by the red circle. The darkish area corresponds to Fe_2O_3 nanoparticles, while the gray-colored regions represent the P(2MA) particles. Figure 1(d) presents the selected area electron diffraction (SAED) distribution of the nanohybrid, confirming the presence of polycrystalline structures. The diffraction rings observed in the SAED pattern align closely with the crystalline planes of the Fe_2O_3/P(2MA) nanohybrid, specifically corresponding to the (012) plane for Fe_2O_3 and the [67] plane for P(2MA). This correlation is consistent with the XRD results presented in Figure 2 and previous results [5].

3.2 XRD properties

Figure 2 presents the results of the XRD test conducted to examine the crystal structure of the pure P(2MA) and the Fe_2O_3/P(2MA) nanohybrid. For the pure P(2MA), the diffraction peaks at $2\theta = 14°$ and 25° correspond to the parallel and perpendicular periodicities of the polymer backbone, respectively, as depicted in Figure 2(a) [68,69]. The broad peaks in the polymer structure indicate its semi-crystalline nature [68]. The XRD pattern of the Fe_2O_3/P(2MA) nanohybrid, shown in Figure 2(b), confirms the presence of crystalline Fe_2O_3. A series of well-defined diffraction peaks appear at 2θ = 23.8°, 31.0°, 42.0°, 61.5°, 65.7°, 70.6°, and 77.1°. These peaks are indexed to the (012), (1040, (113), (214), (300), (028), and (220) planes, respectively, and are consistent with the standard patterns listed in JCPDS card numbers 86-0550 and 33-0664 [70,71]. These planes are characteristic of Fe_2O_3 and confirm its successful incorporation into the nanohybrid. Additionally, the P(2MA) component, being largely semi-crystalline, does not contribute sharp peaks but may contribute a broad hump around 20°–25°, which is typical of CPs. The retention of sharp Fe_2O_3 peaks indicates that the polymer matrix does not disrupt the crystalline structure of the MO, allowing for effective nanohybrid formation with preserved crystallinity. Figure S2 provides the standard XRD patterns for Card No. JCPDS 86-0550 of Fe_2O_3.

To calculate the crystallite size (CS), the Scherrer equation was utilized as follows:

$$CS = (0.9\lambda)/(\beta \cos \theta), \quad (1)$$

where λ represents the X-ray wavelength (CuKα = 0.15405 nm), θ is the Bragg's angle, and β is the full width

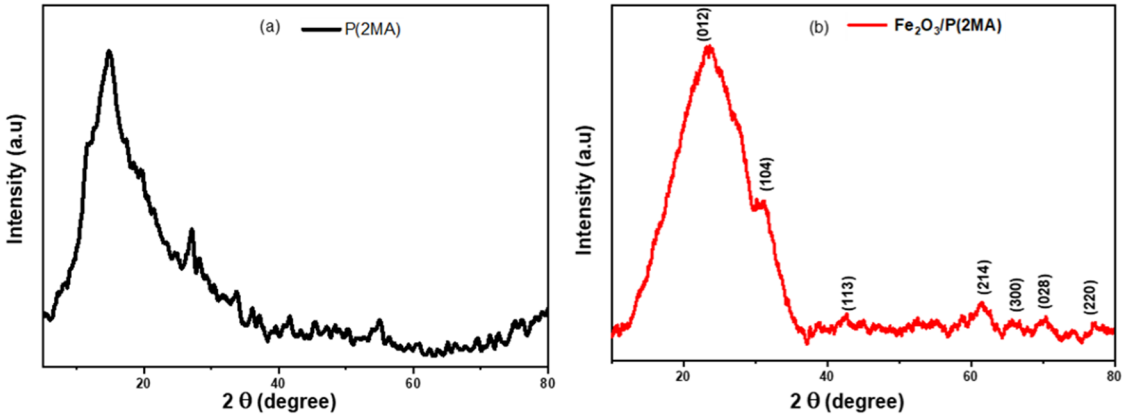

Figure 2: (a) XRD patterns of P(2MA) and (b) the Fe_2O_3/P(2MA) nanohybrid.

at half-maximum [72]. The calculated CS was 3.55 nm for Fe_2O_3/P(2MA).

3.3 FTIR analysis

Figure 3 illustrates the distinctive bands obtained from the FTIR analysis of pure P(2MA) and the Fe_2O_3/P(2MA) nanohybrid. In pure P(2MA), a broad band at 3,423 cm^{-1} corresponds to the stretching vibration of the (–NH–) group. The quinoid ring of pure P(2MA) displays a band at 2,937 cm^{-1}, which indicates C–H stretching vibrations and reflects the polymer's conjugation nature. Additionally, the band at 1,107 cm^{-1} is associated with in-plane C–H bending vibrations [73]. The band at 1,633 cm^{-1} is attributed to C=C stretching vibrations within the conjugated system. C–N stretching vibrations of the benzenoid ring are observed at 1,368 cm^{-1}, while the band at 833 cm^{-1} is contributed by the methyl group attached to the phenyl ring.

The Fe_2O_3/P(2MA) nanohybrid FTIR spectrum reveals characteristic vibrational bands that confirm the successful incorporation of Fe_2O_3 into the polymer matrix. A broad band at 3,222 cm^{-1} is attributed to the N–H stretching vibration of the amine group in P(2MA), which is slightly shifted from that of the pure polymer due to interactions with the Fe_2O_3 nanoparticles [74,75]. The band at 2,972 cm^{-1} corresponds to C–H stretching in the aromatic rings [73]. The peak at 1,590 cm^{-1} indicates C=C stretching vibrations of the quinoid and benzenoid rings, suggesting the preservation of the polymer's conjugated backbone. In contrast, the band at 1,475 cm^{-1} is associated with C–N stretching within the benzenoid unit. The bands at 1,305 cm^{-1}, 1,222 cm^{-1}, and 1,161 cm^{-1} are attributed to in-plane bending of the C–H and C–N bonds, which are sensitive to interactions with MOs [74,75]. The band at 812 cm^{-1} reflects the C–H out-of-plane bending modes, consistent with substituted aromatic rings. Furthermore, the strong band at 594 cm^{-1} is assigned to Fe–O stretching vibrations, confirming the presence of Fe_2O_3 nanoparticles within the polymer matrix [76]. These shifts and the emergence of new bands in the nanohybrid spectrum, compared to pure P(2MA), indicate strong interactions between the polymer and Fe_2O_3, suggesting effective nanohybrid formation that may enhance electron transport and redox behavior.

3.4 Optical properties

The optical spectra of pure P(2MA) and the Fe_2O_3/P(2MA) nanohybrid were analyzed, as shown in Figure S3. In the pure P(2MA) (blue) spectrum, three distinct absorption peaks are observed at approximately 335, 433, and 582 nm. These peaks correspond to the electronic transitions of the benzenoid ring, the P(2MA) emeraldine salt polaron–π* transition, and the excitation at the quinonoid portions, respectively [77,78]. In the case of the Fe_2O_3/P(2MA) nanohybrid, the absorption peak is broader and exhibits higher absorbance across the entire wavelength range. Fe_2O_3 has a broad absorption band in the visible region [79,80]. Consequently, the Fe_2O_3/P(2MA) nanohybrid exhibits a broad absorption band from the UV to the visible and near-infrared (NIR) regions. This suggests that the Fe_2O_3 nanoparticles are well-blended into the polymeric chain, increasing absorption.

The Tauc equation was employed to determine the direct optical bandgap of pure P(2MA) and the Fe_2O_3/P(2MA) nanohybrid as follows [81]:

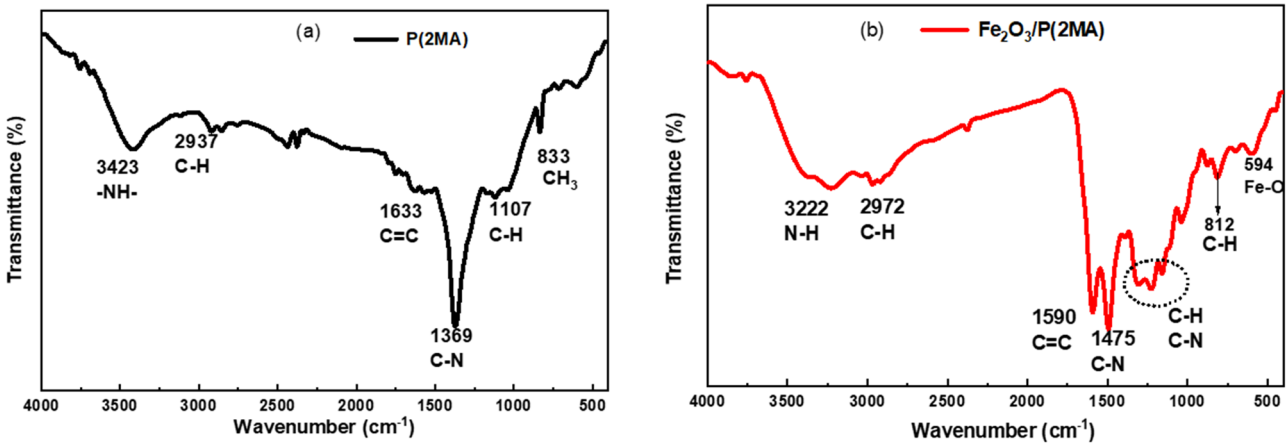

Figure 3: FTIR spectra of (a) P(2MA) and (b) Fe_2O_3/P(2MA) nanohybrid.

$$\alpha E_{ph} = B(E_{ph} - E_g)^{0.5}. \quad (2)$$

Here, α represents the absorption coefficient and E_{ph} represents the energy of the incident light. The constant B represents the absorption threshold width, and E_g denotes the optical bandgap energy [82]. The Tauc plot is presented in Figure 3S. After incorporating Fe_2O_3 nanoparticles, the direct optical bandgap energy of P(2MA) decreases from 2.9 to 2.5 eV, a value consistent with that reported in the literature [76,79]. The electronic interaction between Fe_2O_3 and P(2MA) leads to a reduction in the energy gap of the nanohybrid.

3.5 XPS

Figure 4 illustrates the full XPS spectrum of the Fe_2O_3/P(2MA) nanohybrid to visualize the elemental configuration and bonding state. There are five main peaks. The Fe 2p3 peak is observed at a binding energy of 715.8 eV. A significant C 1s peak is observed at a binding energy of 285.36 eV, with an atomic ratio of 82.85%. Additionally, an O 1s peak is detected at 532.93 eV, and the N 1s peak appears at 399.86 eV, with atomic ratios of 4.69 and 10.57%, respectively. The Cl 2p peak, originating from the iron chloride precursor, is observed at a binding energy of 198.38 eV, with an atomic ratio of 1.43%.

Figure S4 presents the high-resolution XPS spectra of the Fe_2O_3/P(2MA) nanohybrid. Figure S4(a) presents a high-resolution characteristic spectrum of the Fe 2p for the Fe_2O_3/P(2MA) nanohybrid. The Fe 2p peak can be deconvoluted into six peaks. The two peaks with higher atomic ratios, located at 711.97 and 724.64 eV, respectively, correspond to Fe $2p^{3/2}$ and Fe $2p^{1/2}$. These peaks are characteristic of the Fe^{+3} state, indicating the presence of Fe_2O_3 nanoparticles within the polymer chain [43,83]. The high-resolution XPS of the C 1s spectrum is shown in Figure S4(b), and it reveals four different carbon species: C–C/C=C (284.24 eV), C–N (285.17 eV), and C–O (289.19 eV) [84]. The Fe–O bond exhibits a prominent peak in the O 1s spectra at 532 eV, while the O–H group displays a shoulder peak at 531 eV, as depicted in Figure S4(c) [83]. The high-resolution N1s spectra (Figure S4(d)) displayed one peak at 398.6 eV caused by the N–H and C–N bonds associated with the amine (–NH–) groups and cationic species (N^{+}) of P(2MA) [27].

3.6 Electrochemical performance

3.6.1 Galvanostatic charge/discharge profiles

Galvanostatic charge/discharge (CD) testing is performed to determine the charging and discharging time of the electrode material. Additionally, it is used to determine the capacitance of the electrode material. Figure 5 demonstrates the charge/discharge curves of the Fe_2O_3/P(2MA) nanohybrid compared to pure P(2MA) in a 0.5 M HCl solution at 0.4 Ag^{-1}. The total charge/discharge time of P(2MA) is approximately 42 s, while the total charge/discharge time of the Fe_2O_3/P(2MA) nanohybrid is around 670 s.

The electrochemical mechanisms of the Fe_2O_3/P(2MA) nanohybrid involve a combination of faradaic redox reactions from both components, contributing to its high specific capacitance. Iron oxide (Fe_2O_3) plays a critical role by undergoing reversible redox transitions between Fe^{3+} and Fe^{2+} states, contributing significant pseudocapacitance through surface-controlled reactions [85]. Concurrently, P(2MA) participates in rapid and reversible doping/dedoping transitions

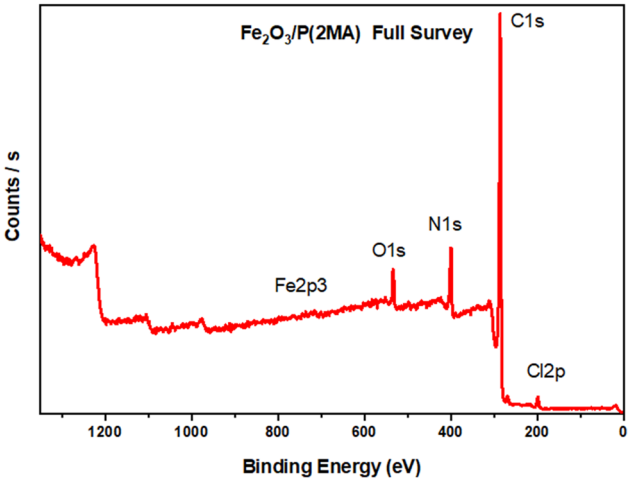

Figure 4: Full survey XPS characterization of the Fe_2O_3/P(2MA) nanohybrid, which showed peaks of Fe 2p, C 1s, O 1s, and N 1s spectra.

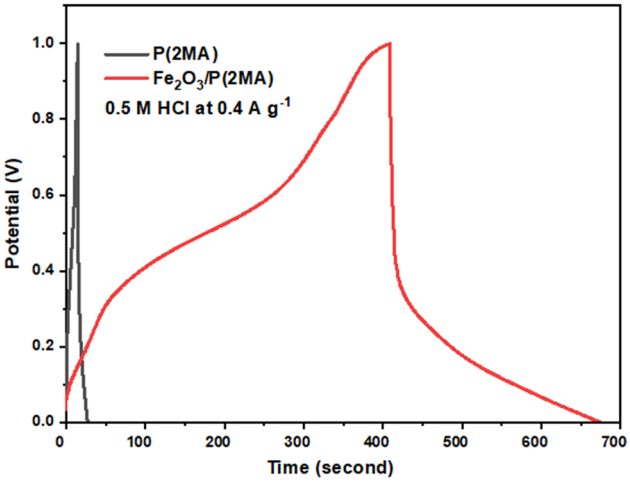

Figure 5: Charge/discharge process of pure P(2MA) and Fe_2O_3/P(2MA) in 0.5 M HCl at 0.4 A g^{-1}.

between its leucoemeraldine, emeraldine, and pernigraniline oxidation states. These transitions contribute additional pseudocapacitive charge storage *via* fast faradaic reactions at the polymer backbone [86]. The associated redox reactions can be summarized as follows:

$$P(2MA) \rightarrow P(2MA)^{+} + e^{-}, \quad (3)$$

$$Fe_2O_3 + H^{+} + e^{-} \rightleftharpoons Fe_3O_4, \quad (4)$$

$$Fe_3O_4 + H^{+} + e^{-} \rightleftharpoons Fe(OH)_2. \quad (5)$$

The Fe_2O_3/P(2MA) nanohybrid morphology, as revealed by TEM and SEM imaging, plays a pivotal role in facilitating these electrochemical mechanisms. The nanohybrid forms a 3D spongy nanofiber network with interconnected meso- and macropores, significantly increasing the electrochemically active surface area. This structure shortens ion-diffusion pathways and enhances electrolyte penetration, both essential for high-rate performance. The *in situ* formation of Fe_2O_3 within the P(2MA) matrix promotes uniform nanoparticle dispersion, preventing agglomeration and ensuring full utilization of the redox-active oxide. Additionally, the intimate polymer–oxide interface, formed during one-pot photopolymerization, minimizes interfacial charge-transfer resistance [87]. The flexible polymer backbone further accommodates volumetric expansion and contraction during cycling, preserving structural integrity and enhancing long-term stability [88]. Hence, the Fe_2O_3/P(2MA) nanohybrid represents a promising candidate for next-generation supercapacitor electrodes.

The electrolyte is crucial for the performance of supercapacitors, as it significantly influences charge transport [89]. It also affects conductivity and capacitance [90,91]. Aqueous electrolytes are widely employed in electrochemical energy storage systems due to their high ionic conductivity, low viscosity, inherent safety, and environmental friendliness compared to organic electrolytes [89,92]. Furthermore, they offer predictable ionic behavior, faster ion diffusion, and reduced fabrication complexity, making them particularly suitable for early-stage materials screening and fundamental electrochemical investigations [91].

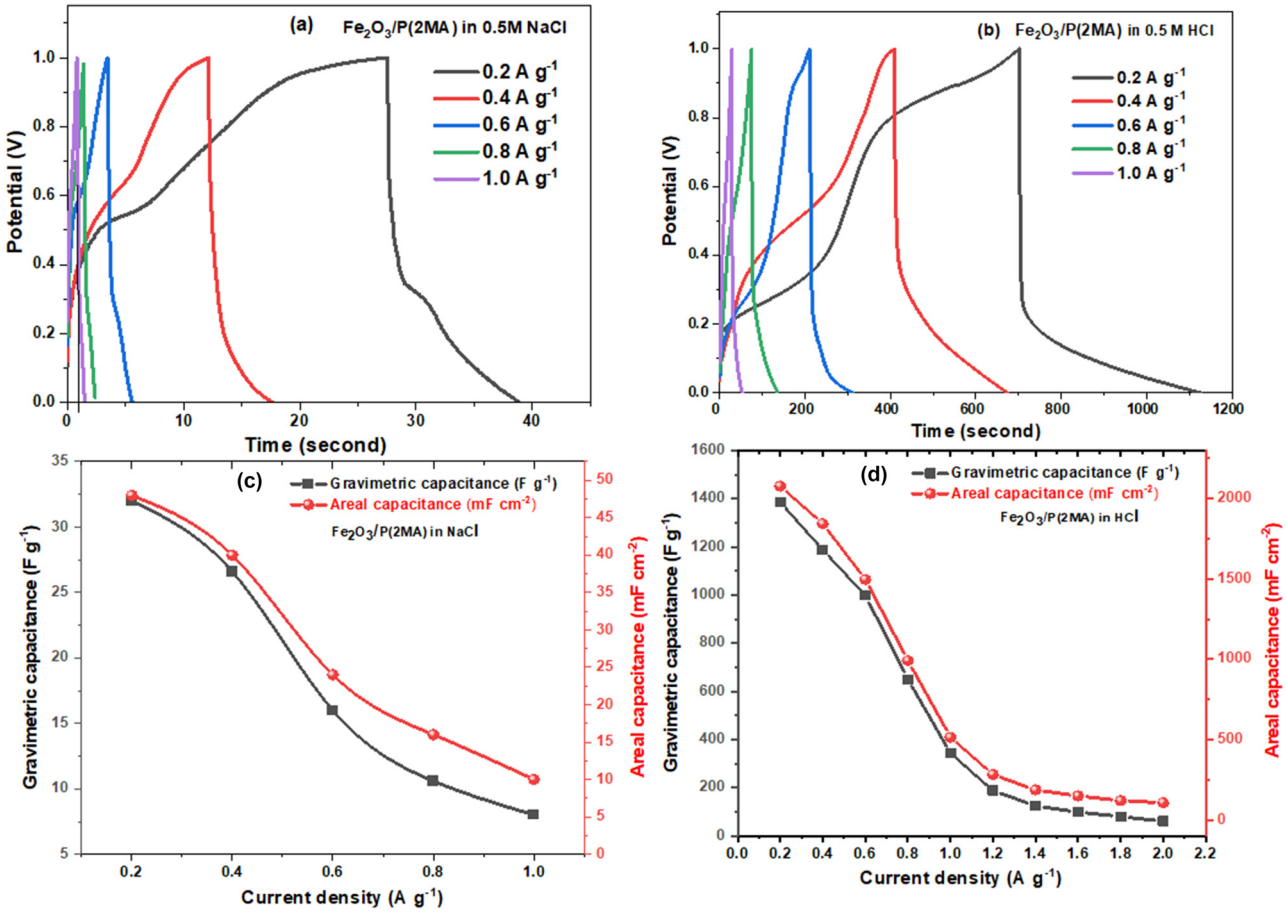

Figure 6: Galvanostatic charge/discharge profiles of Fe_2O_3/P(2MA) were measured at different current densities in (a) 0.5 M NaCl and (b) 0.5 M HCl. The relation between the gravimetric and areal capacitances of Fe_2O_3/P(2MA) in response to various current densities in (c) 0.5 M NaCl and (d) 0.5 M HCl.

Figure 6(a) and (b) illustrates the charge/discharge (CD) behavior profiles of the Fe_2O_3/P(2MA) nanohybrid electrode in two different electrolytic solutions (0.5 M NaCl and 0.5 M HCl). The CD measurements were conducted under various applied current densities ranging from 0.2 to 1.0 A g^{-1}, within a potential window of 0–1 V. The CD curves demonstrate nearly triangular shapes with slight variations in behavior observed in the two electrolytes. This characteristic pattern signifies the presence of pseudocapacitive behavior [93]. This indicates that the charge storage mechanism involves rapid and reversible redox reactions at the interface between the electrode and the electrolyte [94]. The charge/discharge time decreases in the same electrolyte as the current densities increase. Specifically, in the 0.5 M NaCl electrolyte, the charge/discharge time decreases from 37 to 18 s as the current density increases from 0.2 to 0.4 A g^{-1}. This can be attributed to the limited ability of electrolyte ions to access the nanohybrid interior structure, resulting in only the outer active surface being utilized for ion diffusion at higher currents [93,95].

Comparing the discharge time of the nanohybrids in HCl and NaCl at the same current density, it is observed that the discharge time in HCl is higher than that in NaCl, as shown in Figure 6(b). Several factors can explain this. In the NaCl electrolyte, the high surface charge density of Na^+ ions leads to strong interactions with water molecules, resulting in larger hydration spheres and less mobile ions. On the other hand, the H^+ ions in the HCl electrolyte have smaller hydration spheres, which increases their diffusion rates due to their higher kinetic movements. Additionally, the smaller hydration spheres of H^+ ions enable them to penetrate the electrode material, accessing more active regions [90].

Furthermore, H^+ ions have higher ionic conductivity compared to Na^+ ions [16,96,97]. The higher discharge time observed in HCl indicates a higher capacitance and the ability to store more energy in the supercapacitor device. The nature of the GCD shape is a crucial indicator of the charge storage mechanism, directly corresponding to the type of supercapacitor. The Fe_2O_3/P(2MA) nanohybrid demonstrates the characteristics of a nanohybrid supercapacitor, combining both pseudocapacitance and electrical double-layer capacitance (EDLC).

Based on the CD curves, the gravimetric (C_{wt}) and areal (C_A) capacitances of the nanohybrid in NaCl and HCl electrolytes were determined using the following equations [4]:

$$C_{wt} = \frac{4I}{m(\Delta E/\Delta t)}, \tag{6}$$

$$C_A = \frac{4I}{A(\Delta E/\Delta t)}. \tag{7}$$

In the equations, I represent the applied constant current (A), $(\Delta E/\Delta t)$ represents the slope of the discharge curve, A represents the electrode footprint area (cm^{-2}), and m (g) represents the mass of the electroactive material on each electrode [98].

The gravimetric and areal capacitances gradually reduce as the current densities increase. This phenomenon can be attributed to the slow electrochemical activity kinetics observed at higher current densities and the limited ability of most nanohybrids to effectively participate in the electrochemical reactions under these higher current densities. Additionally, increasing current density hinders the charges from having sufficient time to traverse through the pores, decreasing the specific capacitance [99,100].

Figure 6(c,d) illustrates the gravimetric and areal capacitance variation of the Fe_2O_3/P(2MA) nanohybrid at different current densities. The nanohybrid exhibits higher capacitance values at a lower current density (0.2 A g^{-1}). In the NaCl electrolyte, the gravimetric capacitance is approximately 32 F g^{-1}, while the areal capacitance is around 48 mF cm^{-2} at 0.2 A g^{-1}. Conversely, the nanohybrid demonstrates significantly higher capacitance values in the HCl electrolyte (Figure 6d). At a current density of 0.2 A g^{-1}, the gravimetric capacitance reaches approximately 1385.6 F g^{-1}, and the areal capacitance is approximately 2078.5 mF cm^{-2}. Notably, the gravimetric and areal capacitances of the Fe_2O_3/P(2MA) nanohybrid in the HCl electrolyte are much greater than those in the NaCl electrolyte. This substantial increase can be attributed to the considerably longer discharge time observed in the HCl electrolyte. The hydrogen ions in HCl can more effectively penetrate the electrode material and participate in electrochemical reactions compared to sodium ions.

To broaden the scope of the study and enhance its comparative depth across different aqueous electrolytes, the electrochemical performance of the Fe_2O_3/P(2MA) nanohybrid was also evaluated in potassium hydroxide (KOH) as a basic electrolyte, as shown in Figure S5. In 0.5 M KOH, the Fe_2O_3/P(2MA) nanohybrid exhibited a charge/discharge time of approximately 140 s at 0.2 A g^{-1}, corresponding to a gravimetric capacitance of around 30 F g^{-1}. These values are significantly lower than those obtained in 0.5 M HCl electrolyte.

Several studies have investigated polymer-based MO nanohybrids for supercapacitor applications, highlighting their potential in energy storage. Table 1 summarizes the electrochemical performance of some previous works in this field. The Fe_2O_3/P(2MA) nanohybrid demonstrates impressive performance, outperforming or closely

matching other reported materials. It exhibits a specific capacitance of 998.4 F g^{-1} at 0.6 A g^{-1} in 0.5 M HCl, with 99.9% retention after 2,000 cycles. For instance, a P(2MA)/Ag–Ag_2O nanocomposite achieved 443 F g^{-1} at 0.4 A g^{-1} with 89.9% retention after 1,000 cycles [5], while a poly (*m*-toluidine)/Co–Ni oxide system reached 308 F g^{-1} at 0.6 A g^{-1} with 98% retention after 1,000 cycles [27]. A PANI/α-Fe_2O_3 nanohybrid recorded 473.6 F g^{-1} at 1 A g^{-1} and 98.2% retention over 5,000 cycles in 1 M Na_2SO_4 [101], while the PPy/Fe_2O_3 nanocomposite reported a capacitance of 395 F g^{-1} [67]. These results demonstrate that the proposed Fe_2O_3/P(2MA) nanohybrid delivers a remarkable combination of high capacitance and excellent cycling durability. This positions it as a competitive and viable candidate for next-generation supercapacitor technologies.

3.6.2 CV profiles

Figure S6 presents the CV curves of P(2MA) and Fe_2O_3/P(2MA) electrodes. The CV curve was recorded at a scan rate of 30 mV/s in 0.5 M HCl electrolyte over a potential window of 0.0–1.0 V. The Fe_2O_3/P(2MA) electrode exhibits a significantly higher current response and a larger enclosed area under the CV curve than the pure P(2MA) electrode. The reaction rate of an electrochemical process is proportional to the electrochemically active surface area (ECSA) of the electrode, as a larger surface area provides more active sites for the reaction. The ECSA of an electrode can be evaluated using CV, where a greater area under the CV curve typically indicates a larger surface area [27,49]. This result suggests that the spongy structure of the Fe_2O_3/P(2MA) electrode contributes to its high surface area, leading to superior charge storage capacity and specific capacitance.

Figure 7(a) and (b) depicts the CV of the Fe_2O_3/P(2MA) nanohybrid in NaCl and HCl electrolytes within a voltage range of 0–1 V, using different scan rates ranging from 30 to 500 mV/s. The surface area under the CV curve increases with an increase in the scan rate, indicating the desired capacitive behavior of the electrode. At higher scan rates, the diffusion rate of electrolytic ions becomes more significant than the reaction rate. As a result, many electrolytic ions reach the electrode/electrolyte interface, while only a tiny fraction of these ions participate in the charge transfer reaction. According to the Randles–Sevcik equation, this increases the peak current in the CV curve and the area under the CV curve at higher scan rates. The slow scan rate provides sufficient time for the electrolyte to penetrate all of the pores and fully interact with the electrode. In the HCl electrolyte, the CV curves of the nanohybrid exhibit stronger oxidation and reduction currents compared to NaCl at the same scan rates, as shown in Figure 7(a,b).

Moreover, the HCl electrolyte shows a larger surface area under the CV curve, indicating enhanced electrochemical activity in HCl. This observation suggests that the specific cationic species in the electrolyte solution play a crucial role in these electrochemical processes. As seen in Figure 7(b), the integral area of the CV curve for the Fe_2O_3/P(2MA) nanohybrid in 0.5 M HCl at a scan rate of 500 mV/s is significantly larger. This result indicates a greater capacity for electrochemical energy storage in the HCl electrolyte.

The following equation is used to determine specific capacitance based on CV data [107,108]:

$$C_{\mathrm{wt}} = \frac{4}{msV}\int_{v_1}^{v_n} i\mathrm{d}v, \tag{8}$$

where $\int_{v_1}^{v_n} i\mathrm{d}v$ represents the integrated area under the CV curve, s represents the scan rate (V/s) applied, and the active material mass on each electrode is denoted m(g). ΔV is double the potential range covered in the CV measurement. It starts from V1, reaches V2, and then returns to V1. At a scan rate of 500 mV/s, the specific

Table 1: Electrochemical performance of supercapacitor electrode materials based on the polymer and MO

Nanomaterial	Current density (A g^{-1})	Electrolyte	Specific capacitance (F g^{-1})	Ref.
PMT/Ag–Ag_2O	0.4	0.5 M HCl	443	[5]
PMT/(Co–Ni)	0.6	0.5 M HCl	308	[27]
PANI/α-Fe_2O_3	1	1.0 M Na_2SO_4	473.6	[101]
PANI/α-Fe_2O_3	0.2	1.0 M H_2SO_4	857	[102]
Fe_2O_3@PPy	—	3 M KOH	395.45	[67]
Fe_2O_3/poly-2 aminothiophenol	0.3	1.0 M NaOH	46.4	[103]
Fe_2O_3/PPy/carbon cloth	—	1.0 M Na_2SO_4	640	[104]
Carbon foam/Fe_2O_3	0.2	6.0 M KOH	225	[105]
N-doped carbon nanofiber/Fe_3C/Fe_2O_3	2	2.0 M KOH	590.1	[106]
Fe_2O_3/P(2MA)	0.6	0.5 M HCl	998.4	This work

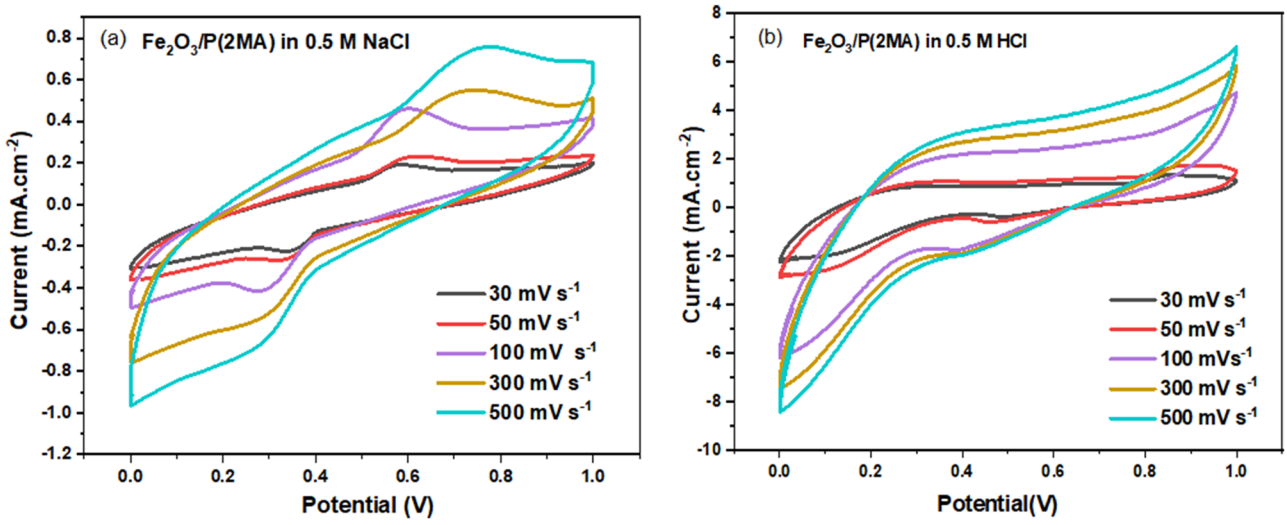

Figure 7: CV in (a) 0.5 M NaCl and (b) 0.5 M HCl at different scan rates for the Fe_2O_3/P(2MA) nanohybrid.

capacitance of the nanohybrid in 0.5 M NaCl electrolyte was determined to be 51.4 F g^{-1} using the CV integral area. In contrast, the specific capacitance of the nanohybrid was measured to be significantly higher at 225 F g^{-1} in a 0.5 M HCl electrolyte.

3.6.3 Ragone plot

The Ragone plot is a graphical representation used to compare the energy density of various energy storage devices. It shows the amount of energy that can be stored relative to the power output of each device. In this plot, the specific energy (energy per unit mass) is plotted on the vertical axis, while the specific power (power per unit mass) is plotted on the horizontal axis. The Ragone plot is utilized to examine the electrochemical performance of the Fe_2O_3/P(2MA) nanohybrid electrode in NaCl and HCl electrolytic solutions, as presented in Figure 8(a) and (b). The specific energy and power of the nanohybrid electrode can be calculated using the following equations [109,110]:

$$E_{wt}(\text{W hkg}^{-1}) = 0.0347 C_{wt}(\Delta E)^2, \tag{9}$$

$$P_{wt}(\text{W kg}^{-1}) = 3{,}600\left(\frac{E_{wt}}{\Delta t}\right). \tag{10}$$

Here, ΔE represents the discharge potential after considering the IR drop, and Δt denotes the discharge time. In the NaCl electrolyte, the Fe_2O_3/P(2MA) nanohybrid electrode exhibits average specific energy and power values of 0.13 and 180 W kg^{-1}, respectively. However, higher values

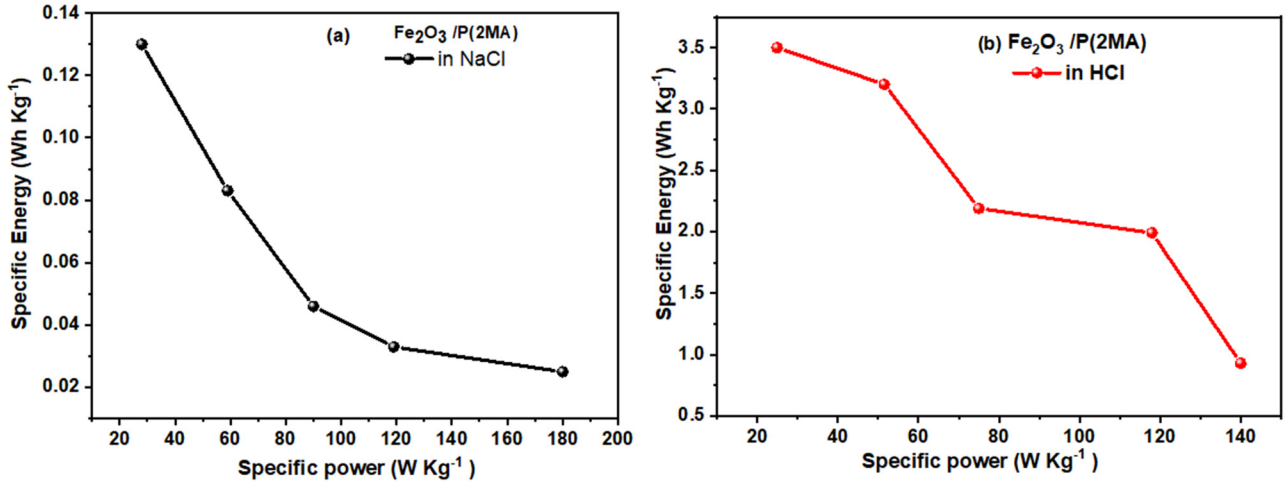

Figure 8: Ragon plot profile of the Fe_2O_3/P(2MA) nanohybrid in (a) NaCl and (b) HCl electrolytes.

of 3.5and 140 W kg^{-1} are obtained using the HCl electrolyte. Utilizing the Fe_2O_3/P(2MA) nanohybrid in an HCl electrolyte for energy storage is more efficient. This is primarily due to the material's significantly higher specific energy than its NaCl counterpart.

3.6.4 Impedance

Electrochemical impedance spectroscopy (EIS) is a versatile technique for analyzing electrochemical systems, offering insights into charge transfer rates, redox reactions, diffusion processes, and capacitive behavior. EIS expresses impedance as a combination of real and imaginary components, commonly visualized using a Nyquist plot, where the real impedance is plotted on the *X*-axis and the negative imaginary impedance on the *Y*-axis [111]. Figure 9(a) presents the Nyquist plot of the Fe_2O_3/P(2MA) nanohybrid electrode, recorded over a frequency range from 10 MHz to 100 kHz in a 0.5 M HCl electrolyte. The plot employs orthonormal scaling for clear visualization. In the low-frequency region, the Nyquist plot exhibits nearly linear behavior (right side of the plot). At the same time, a distinct semicircular arc appears in the high-frequency region (left side of the plot). The diameter of the semicircle corresponds to the charge-transfer resistance, while the slope of the low-frequency tail reflects ion transport through the electrode/electrolyte interface [112].

The EIS data were fitted using the EC-Lab software to a modified Randle's circuit comprising four resistive elements, one double-layer capacitance, and two constant phase elements. The extracted values, listed in Table S1, help interpret the physical and electrochemical processes occurring in the electrode. R_1 (2.473 Ω) represents the solution resistance, and its low value confirms the good ionic conductivity of the electrolyte. R_2 (0.10 Ω) corresponds to the charge-transfer resistance at the polymer–electrolyte interface. This very low resistance highlights the strong interfacial coupling between Fe_2O_3 and the conductive P(2MA) matrix, contributing to the nanohybrid's improved electrical conductivity and electrochemical stability [113]. R_3 (49.13 Ω) and R_4 (1,574 Ω) are associated with ion diffusion and faradaic resistance, respectively. The capacitance C_1 (15.56 μF) reflects the double-layer capacitance, indicating good electrochemical interface formation. The constant phase elements Q_1 (2.22 F s) and Q_2 (0.02 mF s) with exponents a_1 (0.55) and a_2 (0.59) represent non-ideal capacitive behavior due to surface roughness and porosity in the electrode structure. Hence, the EIS results strongly support the electrochemical behavior observed in CV and GCD tests and are consistent with the porous nanofiber morphology. These characteristics make the Fe_2O_3/P(2MA) nanohybrid a strong candidate for high-performance electrochemical energy storage systems.

3.6.5 Stability

The cycling stability of the Fe_2O_3/P(2MA) nanohybrid electrode was evaluated in a 0.5 M HCl electrolyte at a specific current density of 0.6 A g^{-1}. The stability was assessed by monitoring the preservation of gravimetric capacitance and the capacitance retention (*y*-axis) in response to charge–discharge cycles for up to 2,000 cycles, as shown in Figure 9(b). The inset in the figure compares the first cycle to the final cycle. The nanohybrid electrode exhibited 100%

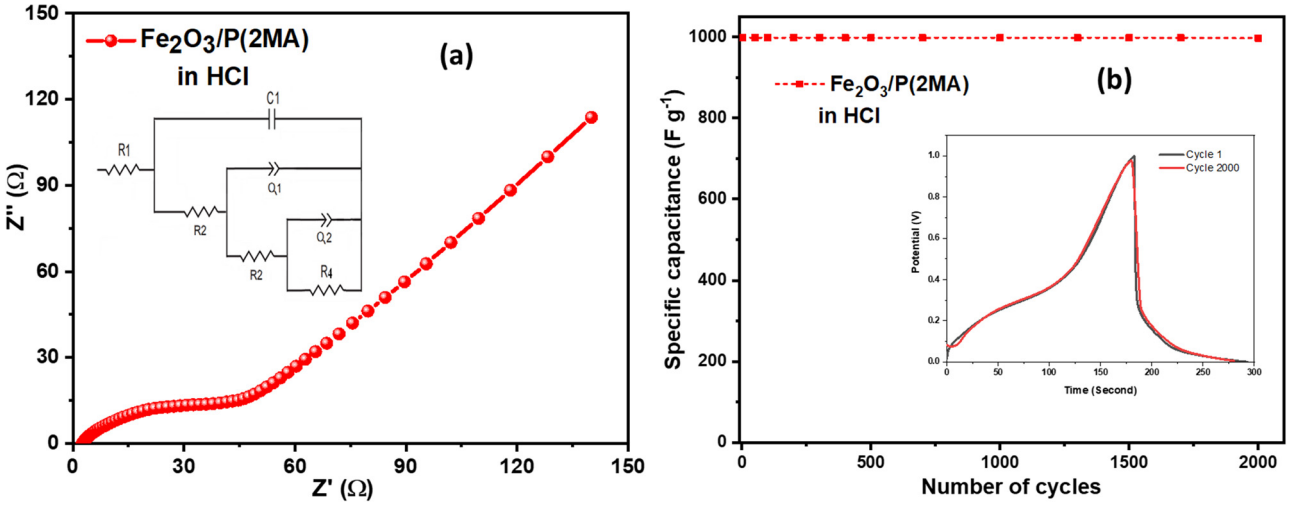

Figure 9: (a) Nyquist plot with equivalent circuit and (b) cyclic stability of the Fe_2O_3/P(2MA) nanohybrid in HCl.

cycling stability during the first 300 cycles. After 2,000 cycles, the nanohybrid electrode achieved a remarkable cycling stability of approximately 99.9% (998 F g^{-1}) compared to its initial specific capacitance of 998.4 F g^{-1} (100%). This implies that the Fe_2O_3/P(2MA) nanohybrid electrode exhibits good cycling electrochemical stability.

The observed long-term cycling stability of the Fe_2O_3/P(2MA) nanohybrid arises from the synergistic interplay between its structural architecture and chemical resilience. The P(2MA) matrix is a redox-active yet chemically robust host. Its intrinsically conductive backbone facilitates rapid charge transfer while preserving the integrity of the polymer chain. As demonstrated by Rahayu *et al.*, P(2MA) maintains high electrical conductivity in 0.5 M HCl without undergoing acid-induced degradation, confirming its electrochemical stability under harsh conditions [114]. Simultaneously, Fe_2O_3 offers corrosion resistance, substantially reducing the risk of metal-ion leaching during prolonged operation. As confirmed by TEM and SEM imaging, the formation of a spongy nanofiber architecture in the Fe_2O_3/P(2MA) matrix reveals that Fe_2O_3 nanoparticles are tightly embedded within the polymer framework. This structure reflects strong interfacial adhesion between Fe_2O_3 and P(2MA), which effectively suppresses nanoparticle agglomeration, mitigates structural disintegration, and reduces the risk of mechanical detachment during repetitive redox cycling.

Furthermore, the flexible polymeric scaffold accommodates volumetric changes during Fe^{3+}/Fe^{2+} redox transitions, preventing microcracking during long-term cycling. Notably, the polymer matrix also serves as a protective sheath, shielding Fe_2O_3 from direct contact with the acidic electrolyte and enhancing the overall system stability [115]. This architectural strategy aligns with previous studies that demonstrate improved durability of MOs encapsulated in polymer matrices [27,115–117]. Using 0.5 M HCl as the electrolyte maximizes capacitance and helps mitigate localized electrolyte depletion at the electrode-electrolyte interface. The low charge-transfer resistance observed from EIS measurements, even after 2,000 cycles, indicates that the electronic and ionic transport pathways remain unobstructed, thereby validating the structural and electrochemical integrity of the nanohybrid over prolonged cycling. Additionally, the device was meticulously sealed to prevent any electrolyte loss due to evaporation (Figure S7), ensuring stable ionic conductivity throughout the testing period. This suggests that the Fe_2O_3/P(2MA) nanohybrid electrode is highly suitable as an effective electrode material in supercapacitor applications.

The post-PEC SEM analysis confirmed the structural integrity of the Fe_2O_3/P(2MA) nanohybrid after the electrochemical measurements, as illustrated in Figure S8. The electrode maintained its morphology with no microcracking or particle agglomeration. Additionally, it remained well-adhered to the substrate without degradation. These observations indicate strong corrosion resistance and affirm the long-term mechanical stability of the electrode.

The superior performance of the Fe_2O_3/P(2MA) nanohybrid arises from multiple synergistic factors, as supported by structural, morphological, and electrochemical evidence. P(2MA) provides a highly conductive polymeric backbone enriched with redox-active sites. A methyl substituent enhances charge delocalization and offers steric protection against overoxidation. The flexible polymer chains also buffer volumetric fluctuations during charge–discharge cycling, contributing to mechanical stability and improved capacitance retention [98]. Fe_2O_3 offers high theoretical capacitance due to its reversible $Fe^{3+/}Fe^{2+}$ redox transitions, but is limited by low electrical conductivity and a tendency to agglomerate when used alone. However, when Fe_2O_3 nanoparticles are generated *in situ* during photopolymerization and uniformly embedded within the P(2MA) matrix, they contribute significant pseudocapacitance while avoiding aggregation. This integration results in an interpenetrating nanofiber network with high surface area, shortened ion-diffusion pathways, and improved electrolyte accessibility to active sites [22]. SEM and TEM analyses confirm the spongy nanostructure, which is crucial for rapid ion transport and enhanced rate capability. Furthermore, the one-pot photopolymerization process ensures intimate polymer–oxide interfacial contact, reducing interfacial resistance and enhancing electron mobility. The EIS supports this finding, showing low charge-transfer resistance, indicative of efficient charge transport within the nanohybrid structure.

4 Conclusions

This work successfully presents a one-pot photopolymerization strategy for synthesizing Fe_2O_3/P(2MA) nanohybrid aimed at high-performance supercapacitor applications. The iron precursor acts dually as both the oxidant and the source of Fe_2O_3, simplifying fabrication while promoting strong polymer–oxide integration. The combination of photochemical and oxidative polymerization successfully yields robust, interpenetrating Fe_2O_3/P(2MA) spongy nanofibers, as confirmed by structural and morphological analyses. The resulting architecture exhibits excellent electrochemical performance. Tests were conducted

in HCl, KOH, and NaCl electrolytes. The Fe_2O_3/P(2MA) nanohybrid delivers a specific capacitance of 998.4 F g^{-1} at 0.6 A g^{-1} in 0.5 M HCl, with energy and power densities of 3.5 W hkg^{-1} and 140 W kg^{-1}, respectively. Remarkably, it retains 99.9% of its initial capacitance after 2,000 cycles, demonstrating exceptional long-term stability. These findings underscore the novelty, effectiveness, and scalability of the synthesis method, establishing Fe_2O_3/P(2MA) as a promising electrode material for next-generation supercapacitor technologies.

Funding information: This work was supported and funded by the Deanship of Scientific Research at Imam Mohammad Ibn Saud Islamic University (IMSIU) (grant number IMSIU-DDRSP2503).

Author contributions: A.M. Ahmed: writing – review and editing, software, visualization, and funding acquisition. D. Essam: methodology, writing – original draft, visualization, and software. M.A. Basyooni-M. Kabatas: review and editing, formal analysis, data curation, and software. A.A. Abdel-Khaliek: investigation, supervision, and formal analysis. M. Shaban: resources, visualization, and validation. M.J. Aljaafreh: data curation, visualization, and formal analysis. M. Rabia: conceptualization, supervision, and writing – review and editing. All authors have accepted responsibility for the entire content of this manuscript and approved its submission.

Conflict of interest: The authors state no conflict of interest.

Data availability statement: The datasets generated and/or analyzed during the current study are available from the corresponding author on reasonable request.

References

[1] Abdah MAAM, Azman NHN, Kulandaivalu S, Sulaiman Y. Review of the use of transition-metal-oxide and conducting polymer-based fibres for high-performance supercapacitors. Mater Des. 2020;186:108199.

[2] Mao X, Liu H, Xu J, Mengwei L, Yang W. Surface reconstruction of Co3O4/rGO heterointerface enabling high-performance asymmetric supercapacitors. J Energy Storage. 2024;102:114128.

[3] Thalji MR, Ali GAM, Shim J-J, Chong KF. Cobalt-doped tungsten suboxides for supercapacitor applications. Chem Eng J. 2023;473:145341.

[4] Atta A, Abdelhamied MM, Essam D, Shaban M, Alshammari AH, Rabia M. Structural and physical properties of polyaniline/silver oxide/silver nanocomposite electrode for supercapacitor applications. Int J Energy Res. 2022;46(5):6702–10.

[5] Essam D, Ahmed AM, Abdel-khaliek AA, Shaban M. One pot synthesis of poly m-toluidine incorporated silver and silver oxide nanocomposite as a promising electrode for supercapacitor devices. 2025;15:2698.

[6] Huang Y, Li H, Wang Z, Zhu M, Pei Z, Xue Q, et al. Nanostructured Polypyrrole as a flexible electrode material of supercapacitor. Nano Energy. 2016;22:422–38. doi: 10.1016/j.nanoen.2016.02.047.

[7] Afif A, Rahman SM, Tasfiah Azad A, Zaini J, Islam MA, Azad AK. Advanced materials and technologies for hybrid supercapacitors for energy storage – A review. J Energy Storage. 2019;25(July):100852. doi: 10.1016/j.est.2019.100852.

[8] Karri SN, Ega SP, Perupogu V, Srinivasan P. Enhancing the electrochemical performance of polyaniline using fly ash of coal waste for supercapacitor application. ChemistrySelect. 2021;6(10):2576–89.

[9] Sun J, Luo B, Li H. A review on the conventional capacitors, supercapacitors, and emerging hybrid ion capacitors: past, present, and future. Adv Energy Sustainable Res. 2022;3(6):2100191.

[10] Mao X, Hatton T, Rutledge G. A review of electrospun carbon fibers as electrode materials for energy storage. Curr Org Chem. 2013;17(13):1390–401.

[11] Shoeb M, Fouzia M, Khan MN, Kim B-J, Jeong C. Waste to energy strategy: Graphene-supported Au-Ag_2O polyIndole nanocomposites for antimony adsorption and their sequential utilization in supercapacitors device. Sep Purif Technol. 2024;329:123080.

[12] Zhou Q, Wei T, Yue J, Sheng L, Fan Z. Polyaniline nanofibers confined into graphene oxide architecture for high-performance supercapacitors. Electrochim Acta. 2018;291:234–41. doi: 10.1016/j.electacta.2018.08.104.

[13] Kim BH, Kim CH, Yang KS, Rahy A, Yang DJ. Electrospun vanadium pentoxide/carbon nanofiber composites for supercapacitor electrodes. Electrochim Acta. 2012;83:335–40. doi: 10.1016/j.electacta.2012.07.093.

[14] Guo FM, Xu RQ, Cui X, Zhang L, Wang KL, Yao YW, et al. High performance of stretchable carbon nanotube-polypyrrole fiber supercapacitors under dynamic deformation and temperature variation. J Mater Chem A. 2016;4(23):9311–8.

[15] Balan BK, Chaudhari HD, Kharul UK, Kurungot S. Carbon nanofiber-RuO2-poly(benzimidazole) ternary hybrids for improved supercapacitor performance. RSC Adv. 2013;3(7):2428–36.

[16] Radhamani AV, Shareef KM, Rao MSR. ZnO@MnO2 core-shell nanofiber cathodes for high performance asymmetric supercapacitors. ACS Appl Mater Interfaces. 2016;8(44):30531–42.

[17] Yang Y, Yang F, Hu H, Lee S, Wang Y, Zhao H, et al. Dilute NiO/carbon nanofiber composites derived from metal organic framework fibers as electrode materials for supercapacitors. Chem Eng J. 2017;307:583–92.

[18] Zhou H, Liu Y, Ren M, Zhai HJ. Mechanically exfoliated graphite paper with layered microstructures for enhancing flexible electrochemical energy storage. Inorg Chem Front. 2022;9:1346–57.

[19] Bashir T, Shakoor A, Ahmed E, Niaz NA, Akhtar MS, Raza MR, et al. Polypyrrole-Fe2O3 Nanocomposites with high dielectric constant: In situ chemical polymerisation. Polym Polym Compos. 2018;26(3):233–41.

[20] Liao M, Zhang K, Yan W, Yue H, Luo C, Wu G, et al. Constructing amorphous/crystalline heterointerface in cobalt sulfide for

high-performance supercapacitors. J Power Sources. 2025;625:235663.
[21] Gamal A, Shaban M, BinSabt M, Moussa M, Ahmed AM, Rabia M, et al. Facile fabrication of polyaniline/pbs nanocomposite for high-performance supercapacitor application ahmed. Micromachines. 2022;1:17.
[22] Ahmad SA, Fouzia M, Ansari MA, Alothman AA, Shoeb M, Jeong C. Morus alba-mediated defect-rich Fe-doped V2O5 nanoparticles on woven carbon fiber for high-performance supercapacitor with enhanced charge storage mechanism. J Alloy Compd. 2025;1020:179515.
[23] Fouzia M, Shoeb M, Khan JA, Gondal MA, Jeong C. Chemical reduction-induced defect-rich and synergistic effects of reduced graphene oxide based Cu-doped NiO nanocomposite (RGO@Cu-NiO NCs) decorated on woven carbon fiber for supercapacitor device and their charge storage mechanism. J Energy Storage. 2024;104:114578.
[24] Mohd Abdah MAA, Azman NHN, Kulandaivalu S, Sulaiman Y. Review of the use of transition-metal-oxide and conducting polymer-based fibres for high-performance supercapacitors. Mater Des. 2020;186:108199. doi: 10.1016/j.matdes.2019.108199
[25] Lu XF, Chen XY, Zhou W, Tong YX, Li GR. α-Fe_2O_3@PANI core–shell nanowire arrays as negative electrodes for asymmetric supercapacitors. ACS Appl Mater Interfaces. 2015;7(27):14843–50.
[26] Shinde SK, Karade SS, Truong NTN, Veer SS, Shaikh SF, Al-Enizi AM, et al. Highly stable and thin layer of conducting PANI decorative on porous 3D nanoflakes like-$NiCo_2O_4$/CF nanomaterials for efficient Hybrid Supercapacitors application. J Energy Storage. 2023;78:109960.
[27] Fathy A, Ahmed AM, Ghanem MA, Hamdy H, Shaban M, Mohammed KMH, et al. Supercapacitance performance of novel core/shell poly (m-toluidine)/(Co-Ni) nanoplatelets/nanoneedles nanocomposite. J Mol Liq. 2023;386:122466.
[28] Bathula C, Reddy R, Naik S, Naushad M, Kim H. Deep eutectic solvent-assisted synthesis of transition metal oxide and its integration into polymer matrix for supercapacitor. J Mol Liq. 2024;403(March):124899. doi: 10.1016/j.molliq.2024.124899.
[29] Li Y, Zhang Z, Chen Y, Chen H, Fan Y, Li Y, et al. Facile synthesis of a Ni-based NiCo2O4-PANI composite for ultrahigh specific capacitance. Appl Surf Sci. 2020;506:144646.
[30] Dhineshkumar S, Rajkumar S, Sathiyan A, Merlin JP. Fabrication of Ag 2 WO 4/PANI composite with enhanced supercapacitor performance. J Mater Sci Mater Electron. 2024;35(20):1–15. doi: 10.1007/s10854-024-13202-2.
[31] Sivakumar C, Nian J, Teng H. Poly (o -toluidine) for carbon fabric electrode modification to enhance the electrochemical capacitance and conductivity. J Power Sources. 2005;144:295–301.
[32] Andriianova AN, Biglova YN. Effect of structural factors on the physicochemical properties of functionalized polyanilines. 2020;10:7468–91.
[33] Bober P, Trchová M, Prokeš J, Varga M, Stejskal J. Polyaniline–silver composites prepared by the oxidation of aniline with silver nitrate in solutions of sulfonic acids. Electrochim Acta. 2011;56(10):3580–5.
[34] Rabia M, Elsayed AM, Alnuwaiser MA. Decoration of poly-3-methyl aniline with As (III) oxide and hydroxide as an effective photoelectrode for electroanalytical photon sensing with photodiode-like behavior. Micromachines. 2023;14(iii).
[35] Abdelazeez AAA, Hadia NMA, Mourad AI, El-fatah GA, Shaban M, Ahmed AM, et al. Effect of Au plasmonic material on Poly M-toluidine for photoelectrochemical hydrogen generation from sewage water. Polymers. 2022;14:17.
[36] Pujari SS, Bobade RG, Shaikh SF, Al-Enizi AM, Ambare RC, Lokhande BJ. A binderless Ru:α-Fe_2O_3 binary nanocomposite electrode for supercapacitor applications. J Mater Sci Mater Electron. 2024;35:2162–75.
[37] Sephra PJ, Baraneedharan P, Sivakumar M, Thangadurai TD, Nehru K. In situ growth of hexagonal-shaped α-Fe_2O_3 nanostructures over few layered graphene by hydrothermal method and their electrochemical performance. J Mater Sci Mater Electron. 2018;29(8):6898–908.
[38] Shaban M, Binsabt M, Ahmed AM. Recycling rusty iron with natural zeolite heulandite to create a unique nanocatalyst for green hydrogen production. Nanomaterials. 2021;11(12):3445.
[39] Phakkhawan A, Suksangrat P, Srepusharawoot P, Ruangchai S, Pawinee K, Pimanpang S, et al. Reagent-and solvent-mediated Fe_2O_3 morphologies and electrochemical mechanism of Fe_2O_3 supercapacitors. J Alloy Compd. 2022;919:165702.
[40] Lu PA, Manikandan MR, Yang PF, He YL, Yang F, Dang ST, et al. Synthesis, analysis and characterization of alpha-Fe_2O_3 nanoparticles and their applications in supercapacitors. 2023;826:1–13.
[41] Singh U, Ramadesigan V, Chakraborty AK, Shukla S, Saxena S. High-performance α-Fe_2O_3 nano cubes as anode for supercapacitors. J Energy Storage. 2024;102:114124.
[42] Ponnarasi K, Elangovan P, Surender S. Results in chemistry development of CNT/Fe_2O_3 nanocomposites as electrode materials for advanced supercapacitors. Results Chem. 2024;7(December 2023):101355. doi: 10.1016/j.rechem.2024.101355.
[43] Palem RR, Ramesh S, Yadav HM, Kim JH, Sivasamy A, Kim HS, et al. Nanostructured Fe2O3@nitrogen-doped multiwalled nanotube/cellulose nanocrystal composite material electrodes for high-performance supercapacitor applications. J Mater Res Technol. 2020;9(4):7615–27. doi: 10.1016/j.jmrt.2020.05.058.
[44] Guo G, Su Q, Zhou W, Wei M, Wang Y. Cycling stability of Fe_2O_3 nanosheets as supercapacitor sheet electrodes enhanced by $MgFe_2O4$ nanoparticles. RSC Adv. 2023;13(6):3643–51.
[45] Lorkit P, Panapoy M, Ksapabutr B. Iron oxide-based supercapacitor from ferratrane precursor via sol-gel-hydrothermal process. Energy Proc. 2014;56(C):466–73.
[46] Azimov F, Kim J, Choi SM, Jung HM. Synergistic effects of Fe_2O_3 nanotube/polyaniline composites for an electrochemical supercapacitor with enhanced capacitance. Nanomaterials. 2021;11(6):1557.
[47] Nandagudi A, Nagarajarao SH, Santosh MS, Basavaraja BM, Malode SJ, Mascarenhas RJ. Hydrothermal synthesis of transition metal oxides, transition metal oxide/carbonaceous material nanocomposites for supercapacitor applications. Mater Today Sustainable. 2022;19:100214.
[48] ur Rehman MN, Munawar T, Nadeem MS, Mukhtar F, Maqbool A, Riaz M, et al. Facile synthesis and characterization of conducting polymer-metal oxide based core-shell PANI-Pr_2O–NiO–Co_3O_4 nanocomposite: As electrode material for supercapacitor. Ceram Int. 2021;47(13):18497–509.
[49] Zhu P, Zhao Y. Cyclic voltammetry measurements of electroactive surface area of porous nickel: Peak current and peak charge methods and diffusion layer effect. Mater Chem Phys. 2019;233:60–7.
[50] Hwang JJ, Soto C, Lafaurie D, Stephen M, Sarno DM. Porous microspheres of polyaniline, poly(o-toluidine), and

poly(m-toluidine) prepared from double emulsions stabilized by toluidine isomers as the single surfactant. J Colloid Interface Sci. 2018;513:331–41. doi: 10.1016/j.jcis.2017.11.029.
[51] Ramli RA. Hollow polymer particles: A review. RSC Adv. 2017;7(83):52632–50.
[52] Lu Y, Chen C, Zhang X. Functional Nanofibers for Energy Storage. In: Handbook of smart textiles. Singapore: Springer; 2015. p. 513–47.
[53] Dhahebi A, Convergence N, Mohammed A, Dhahebi A, Chandra S, Gopinath B. Graphene impregnated electrospun nanofiber sensing materials: a comprehensive overview on bridging laboratory set - up to industry. Nano Convergence. 2020;7:27. doi: 10.1186/s40580-020-00237-4.
[54] Li Y, Fu Z, Su B. Hierarchically structured porous materials for energy conversion and storage. Adv Funct Mater. 2012;22(22):4634–67.
[55] Manuscript A. Environmental Science.
[56] Article R. Chem Soc Rev materials from energy storage and conversion. 2016.
[57] Han S, Wu D, Li S, Zhang F, Feng X. Porous graphene materials for advanced electrochemical energy storage and conversion devices. Adv Mater. 2014;26(6):849–64.
[58] Feng N, Gao M, Zhong J, Gu C, Zhang Y, Liu B. Stable structure and fast ion diffusion: a flexible MoO_2@carbon hollow nanofiber film as a binder-free anode for sodium-ion batteries with superior kinetics and excellent rate capability. Polymers. 2024;16(11):1452.
[59] Liu M, Zhang P, Qu Z, Yan Y, Lai C, Liu T, et al. Ion battery. Nat Commun. 2019;10:3917. doi: 10.1038/s41467-019-11925-z.
[60] Yang S, Zhao S, Chen S. Chemical science recent advances in electrospinning nano fiber materials for aqueous zinc ion batteries. Chem Sci. 2023;14:13346–66.
[61] Zhang X, Zhang J, Song W, Liu Z. Controllable synthesis of conducting polypyrrole nanostructures. J Phys Chem. 2006;110(3):1158–65.
[62] Pan L, Qiu H, Dou C, Li Y, Pu L, Xu J, et al. Conducting polymer nanostructures: template synthesis and applications in energy storage. 2010;11(7):2636–57.
[63] Ali MA, Kim HH, Lee CY, Soh HS, Lee JG, et al. Effects of the $FeCl_3$ concentration on the polymerization of conductive poly(3,4-ethylenedioxythiophene) thin films on (3-aminopropyl) trimethoxysilane monolayer-coated SiO_2 surfaces. Met Mater Int. 2009;15(6):977–81.
[64] Suhasini A, Kumar KPV, Maiyalagan T. Synthesis, thermal and magnetic behavior of iron oxide-polymer nanocomposites. Sci Eng Compos Mater. 2018;25(1):189–95.
[65] Georgia Institute of Technology. Researchers find new mechanism governing particle growth in nanocomposites. Rockville, MD, USA: ScienceDaily, LLC; 2005. p. 1–4.
[66] Kumar A. Nanoarchitectured transition metal oxides and their composites for supercapacitors. Electrochem Sci Adv. 2022;2(6):e2100187.
[67] Balasubramanian N, Prabhu S, Sakthivel N, Ramesh R. Electrochemical performance of Fe_2O_3@PPy nanocomposite as an effective electrode material for supercapacitor electrochemical performance of Fe_2O_3@PPy nanocomposite as an effective electrode material for supercapacitor. ECS J Solid State Sci Technol. 2022;11(9):091001.
[68] Katowah DF, Hussein MA, Alam MM, Sobahi TR, Gabal MA, Asiri AM, et al. Poly(pyrrole-co-o-toluidine) wrapped $CoFe_2O_4$/R(GO-OXSWCNTs) ternary composite material for Ga^{3+} sensing ability. RSC Adv. 2019;9(57):33052–70.
[69] Mahudeswaran A, Vivekanandan J, Jeeva. A. Synthesis, characterization, optical and electrical properties of nanostructured poly(aniline-co-o-bromoaniline) prepared by in-situ polymerization method. Optik. 2016;127:3984–8.
[70] Haydar MS, Ali S, Mandal P, Roy D, Roy MN, Kundu S, et al. Fe–Mn nanocomposites doped graphene quantum dots alleviate salt stress of Triticum aestivum through osmolyte accumulation and antioxidant defense. Sci Rep. 2023;13(1):1–26. doi: 10.1038/s41598-023-38268-6.
[71] Liu L, Fu S, Lv X, Yue L, Fan L, Yu H, et al. A gas sensor With Fe_2O_3 Nanospheres based on trimethylamine detection for the rapid assessment of spoilage degree in fish. Front Bioeng Biotechnol. 2020;8:567584.
[72] Altowyan AS, Shaban M, Abdelkarem K, El Sayed AM. The impact of co doping and annealing temperature on the electrochemical performance and structural characteristics of SnO_2 nanoparticulate photoanodes. Material. 2022;15(19):6534.
[73] Correa CM, Faez R, Bizeto MA, Camilo FF. One-pot synthesis of a polyaniline-silver nanocomposite prepared in ionic liquid. RSC Adv. 2012;2(7):3088–93.
[74] Annamalai R. Synthesis, characterization and electrical properties of nano metal and metal-oxide doped with conducting polymer composites by in-situ chemical polymerization. MOJ Polym Sci. 2017;1(6):4–7.
[75] Rasheed MH, Hashim FS, Abass KH. Impact of Fe_2O_3 nanoparticles on the spectral and optical properties of electrospun nanofibrous poly vinyl alcohol/poly acrylamide. SSRN Electron J. 2023. doi: 10.2139/ssrn.4403005.
[76] Soflaee F, Farahmandjou M, Firoozabadi TP. Polymer-mediated synthesis of iron oxide (Fe_2O_3) nanorod. Chin J Phys. 2015;53(4):178–86.
[77] Wang H, Wen H, Hu B, Fei G, Shen Y, Sun L, et al. Facile approach to fabricate waterborne polyaniline nanocomposites with environmental benignity and high physical properties. Sci Rep. 2017;7(January):1–12.
[78] Wadatkar NS, Waghuley SA. Characterizing the electro-optical properties of polyaniline/poly(vinyl acetate) composite films as-synthesized through chemical route. Results Surf Interfaces. 2021;4(June):100016. doi: 10.1016/j.rsurfi.2021.100016.
[79] Mirzaei A, Janghorban K, Hashemi B, Hosseini SR, Bonyani M, Leonardi SG, et al. Synthesis and characterization of meso-porous α-Fe_2O_3 nanoparticles and investigation of electrical properties of fabricated thick films. Process Appl Ceram. 2016;10(4):209–18.
[80] Mohamed F, Hassaballa S, Shaban M, Ahmed AM. Highly efficient photocatalyst fabricated from the chemical recycling of iron waste and natural zeolite for super dye degradation. Nanomaterials. 2022;12(2):235.
[81] Alenad AM, Taha TA, Zayed M, Gamal A, Shaaban M, Ahmed AM. Impact of carbon nanotubes concentrations on the performance of carbon nanotubes/zinc oxide nanocomposite for photoelectrochemical water splitting. J Electroanal Chem. 2023;943:117579.
[82] Atta A, Abdelhamied MM, Abdelreheem AM, Berber MR. Flexible methyl cellulose/polyaniline/silver composite films with enhanced linear and nonlinear optical properties. Polymers. 2021;13(8):1–16.

[83] Wang H, Mao J, Zhang Z, Zhang Q, Zhang L, Zhang W, et al. Photocatalytic degradation of deoxynivalenol over dendritic-like α-Fe_2O_3 under visible light irradiation. Toxins. 2019;11(2):1–9.
[84] Zhan T, Ding G, Cao W, Li J, She X, Teng H. Amperometric sensing of catechol by using a nanocomposite prepared from Ag/Ag_2O nanoparticles and N,S-doped carbon quantum dots. Microchim Acta. 2019;186(11):743.
[85] Martins AFN, Diniz FB, Rodrigues AR. Reaction between $Fe^{3+}$and aniline in the synthesis of PANI-γFe_2O_3 and PANI-Fe_3O_4 nanocomposites: Mechanistic studies and evaluation of parameters. Nano-Struct Nano-Objects. 2025;42:101477.
[86] EMI shielding performance of graphene oxide reinforced polyaniline/polystyrene solution cast thin films. Synth Met. 2023;296:117369.
[87] Okafor OB, Popoola API, Popoola OM, Adeosun SO. Review on the recent development on polyaniline and transition metal oxides composite electrode for supercapacitor application. Mater. 2025;6(July 2024):100389. doi: 10.1016/j.nxmate.2024.100389.
[88] Li J, Xu GX. Research progress on applications of hDPSCs in cornea reconstruction. Int Eye Sci. 2017;17:1655–8.
[89] Pal B, Yang S, Ramesh S, Thangadurai V, Jose R. Electrolyte selection for supercapacitive devices: A critical review. Nanoscale Adv. 2019;1(10):3807–35.
[90] Xia L, Yu L, Hu D, Chen GZ. Electrolytes for electrochemical energy storage. Mater Chem Front. 2017;1(4):584–618.
[91] Xiong T, Tan TL, Lu L, Siang W, Lee V, Xue J. Harmonizing energy and power density toward 2.7 v asymmetric aqueous supercapacitor. Adv Energy Mater. 2018;1702630:1–10.
[92] Smiatek J, Heuer A, Winter M. Properties of ion complexes and their impact on charge transport in organic solvent-based electrolyte solutions for lithium batteries: insights from a theoretical perspective. Batteries. 2018;4(4):62.
[93] Kulandaivalu S, Suhaimi N, Sulaiman Y. Unveiling high specific energy supercapacitor from layer-by-layer assembled polypyrrole/graphene oxide|polypyrrole/manganese oxide electrode material. Sci Rep. 2019;9(1):1–10.
[94] Lu L, Xu S, An J, Yan S. Electrochemical performance of CNTs/RGO/MnO2 composite material for supercapacitor. Nanomater Nanotechnol. 2016;6:1–7.
[95] Jiang DB, Zhang BY, Zheng TX, Zhang YX, Xu X. One-pot synthesis of η-Fe2O3 nanospheres/diatomite composites for electrochemical capacitor electrodes. Mater Lett. 2018;215:23–6. doi: 10.1016/j.matlet.2017.12.059.
[96] Goriparti S, Miele E, De Angelis F, Di Fabrizio E, Zaccaria RP, Capiglia. C. Review on recent progress of nanostructured anode materials for Li-ion batteries. J Power Sources. 2014;257:421–43. doi: 10.1016/j.jpowsour.2013.11.103.
[97] Zhu J, Xu Y, Wang J, Lin J, Sun X, Mao S. Effect of various electrolyte cations on electrochemical performance of polypyrrole/RGO based supercapacitors. R Soc Chem. 2015;17(43):28666–73.
[98] Shoeb M, Mashkoor F, Jeong H, Khan MN, Jeong C. Investigating the effect of carbon nanotubes decorated $SmVO_4$-MoS_2 nanocomposite for energy storage enhancement via VARTM-fabricated Solid-state structural supercapacitors using woven carbon fiber. Small. 2025;21(3):e2408283.
[99] Bohinc K, Kralj-Iglič V, Iglič A. Thickness of electrical double layer. Effect of ion size. Electrochim Acta. 2001;46(19):3033–40.
[100] Ratajczak P, Suss ME, Kaasik F, Béguin F. Carbon electrodes for capacitive technologies. Energy Storage Mater. 2019;16:126–45. doi: 10.1016/j.ensm.2018.04.031.
[101] Yang Z, Tang L, Ye J, Shi D, Liu S, Mingqing C. Hierarchical nanostructured α-Fe2O3/polyaniline anodes for high performance supercapacitors. Electrochim Acta. 2018;269:21–29.
[102] Prasanna BP, Avadhani DN, Raghu MS, Yogesh KK. Synthesis of polyaniline/α-Fe_2O_3 nanocomposite electrode material for supercapacitor applications; Mater Today Commun. 2017;12:72–8.
[103] Hameed SA, Ewais HA, Rabia M. Dumbbell-like shape Fe_2O_3/poly-2-aminothiophenol nanocomposite for two-symmetric electrode supercapacitor application. J Mater Sci Mater Electron. 2023;34(14):1–8. doi: 10.1007/s10854-023-10586-5.
[104] Wu C, Pei Z, Lv M, Huang D, Wang Y, Yuan S. Polypyrrole-coated low-crystallinity iron oxide grown on carbon cloth enabling enhanced electrochemical supercapacitor performance. Molecules. 2023;28(1):434.
[105] Wu C, Xiong W, Li H. A novel synthesis of carbon foam@Fe_2O_3 via hydrolysis-driven emulsion polymerization for supercapacitor electrodes. Carbon Lett. 2023;33(7):2327–34. doi: 10.1007/s42823-023-00566-4.
[106] Li L, Xie F, Wu H, Zhu Y, Zhang P, Li Y, et al. N-doped porous carbon-nanofiber-supported Fe_3C/Fe_2O_3 nanoparticles as anode for high-performance supercapacitors. Molecules. 2023;28(15):1–14.
[107] Tao Y, Xie X, Lv W, Tang DM, Kong D, Huang Z, et al. Towards ultrahigh volumetric capacitance: Graphene derived highly dense but porous carbons for supercapacitors. Sci Rep. 2013;3:1–8.
[108] Apelgren P, Amoroso M, Säljö K, Montelius M, Lindahl A, Stridh Orrhult L, et al. 3D Nanoporous graphene films converted from liquid-crystalline holey graphene oxide for thin and high-performance supercapacitors. Mater Today Proc. 2019;27:0–31.
[109] Yu L, Chen GZ. Redox electrode materials for supercapatteries. J Power Sources. 2016;326:604–12. doi: 10.1016/j.jpowsour.2016.04.095.
[110] Benchikh I, Ezzat AO, Sabantina L, Benmimoun Y. Investigation of hybrid electrodes of polyaniline and reduced graphene oxide with bio-waste-derived activated carbon for supercapacitor applications. 2024;16(3):421.
[111] Charmaine L, Hussain I, Ma X, Zhang K. Properties, functions, and challenges: current collectors. Mater today Chem. 2022;26:101152.
[112] Torop J, Summer F, Zadin V, Koiranen T, Jänes A, Lust E, et al. Low concentrated carbonaceous suspensions assisted with carboxymethyl cellulose as electrode for electrochemical flow capacitor. Eur Phys J E. 2019;42(1):17–20.
[113] Zhou J, Li J, Liu K, Lan L, Song H, Chen. X. Free-standing cobalt hydroxide nanoplatelet array formed by growth of preferential-orientation on graphene nanosheets as anode material for lithium-ion batteries. J Mater Chem A. 2014;2:9416–23.
[114] Rahayu I, Eddy DR, Novianty AR, Rukiah, Anggreni A, Bahti H, et al. The effect of hydrochloric acid-doped polyaniline to enhance the conductivity. IOP Conf Ser Mater Sci Eng. 2019;509(1):012051.
[115] Vorobiov VK, Bugrov AN, Kasatkin IA. Effect of α-Fe_2O_3 nanoparticles on the mechanism of charge storage in polypyrrole - based hydrogel. Polym Bull. 2021;78(5):2389–404. doi: 10.1007/s00289-020-03216-1.
[116] Zenasni M, Belhadj H, Kiari M, Alelyani M, Alhailiy AB, Benyoucef A, et al. Synthesis, characterization, and enhanced electrochemical behavior of polypyrrole doped ZrO_2–ZnO electrode materials for supercapacitor applications. Front Energy Res. August: 2023;11.
[117] Das SK, Pradhan L, Jena BK, Basu S. Polymer derived honeycomb-like carbon nanostructures for high capacitive supercapacitor application. Carbon. 2023;213:118214.